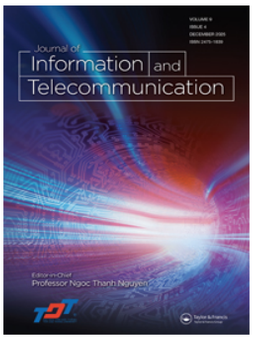

Journal of Information and Telecommunication

ISSN: 2475-1839 (Print) 2475-1847 (Online) Journal homepage: www.tandfonline.com/journals/tjit20

IoT network performance enhancement with intelligent reflecting surfaces and relay

Sang Q. Nguyen, Tran Cong Hung, Bui Trong Hoang, Bui Vu Minh, Yeon Ho Chung & Tan N. Nguyen

To cite this article: Sang Q. Nguyen, Tran Cong Hung, Bui Trong Hoang, Bui Vu Minh, Yeon Ho Chung & Tan N. Nguyen (22 Jan 2026): IoT network performance enhancement with intelligent reflecting surfaces and relay, Journal of Information and Telecommunication, DOI: 10.1080/24751839.2026.2614134

To link to this article: https://doi.org/10.1080/24751839.2026.2614134

Published online: 22 Jan 2026.

JOURNAL OF INFORMATION AND TELECOMMUNICATION
https://doi.org/10.1080/24751839.2026.2614134

IoT network performance enhancement with intelligent reflecting surfaces and relay

Sang Q. Nguyen[a], Tran Cong Hung[b], Bui Trong Hoang[c], Bui Vu Minh[d], Yeon Ho Chung[e] and Tan N. Nguyen [f]

[a]Wireless Communication Laboratory, Posts and Telecommunications Institute of Technology, Ho Chi Minh City, Vietnam; [b]Dean of School of Computer Science & Engineering, The SaiGon Internaltional University, Ho Chi Minh City, Vietnam; [c]Department of Posts and Telecommunications, Hanoi Department of Information and Communications, Ha Noi City, Vietnam; [d]Faculty of Engineering and Technology, Nguyen Tat Thanh University, Ho Chi Minh City, Vietnam; [e]Department of Information and Communications Engineering, Pukyong National University, Busan, South Korea; [f]Advanced Intelligent Technology Research Group, Faculty of Electrical and Electronics Engineering, Ton Duc Thang University, Ho Chi Minh City, Vietnam

ABSTRACT

This article explores the integration of a relay station with two intelligent reflecting surfaces (IRSs) to enhance energy efficiency (EE) and system throughput (ST) in low-power wide-area networks (LPWAN) modelled for Internet of Things (IoT) applications. By leveraging IRS technology, the system improves communication between IoT sensors, the relay station, and the IoT gateway, mitigating signal degradation and optimizing energy consumption. To demonstrate these improvements, we derive theoretical expressions for ST and EE in an LPWAN environment, considering IRS-assisted relay transmission over Nakagami-*m* fading channels. Our analysis demonstrates that incorporating IRSs leads to significant performance enhancements compared to conventional non-IRS systems. More specifically, the proposed network achieves a power reduction of 10 dBm while achieving the same ST and EE targets, highlighting its energy efficiency advantages. Furthermore, our results show that an LPWAN employing a relay station and IRSs is capable of maintaining reliable operation in high-frequency regimes, such as 5 GHz, while maintaining stable communication over distances of up to 200 meters. We conduct an in-depth investigation into the impact of various factors, including the number of reflecting elements, IRS placement, data transmission rate, available bandwidth, and operating frequency, on overall system performance. These insights provide valuable guidelines for the future design and deployment of IRS-assisted IoT frameworks, ensuring efficient, high-performance communication in LPWAN environments.

ARTICLE HISTORY
Received 24 October 2025
Accepted 3 January 2026

KEYWORDS
Intelligent reflecting surfaces; internet of things; relay; energy efficiency; throughput

1. Introduction

Recently, intelligent reflecting surfaces (IRS) and relay stations have recently attracted significant attention as promising technologies to enhance the performance of Internet of

CONTACT Tan N. Nguyen nguyennhattan@tdtu.edu.vn Advanced Intelligent Technology Research Group, Faculty of Electrical and Electronics Engineering, Ton Duc Thang University, Ho Chi Minh City 70000, Vietnam

Things (IoT) networks (V. D. Le et al., 2025; Mahbub & Shubair, 2024; S. Q. Nguyen, Le, Thien, et al., 2024; Quang et al., 2024). An IRS is a planar metasurface composed of a large number of passive or semi-passive reflecting elements (REs) that can intelligently adjust the phase, amplitude, or polarization of incident electromagnetic waves to reconfigure the wireless propagation environment. By appropriately tuning the reflection coefficients, IRS can establish favourable channel conditions, improve signal strength, and reduce interference, thereby enhancing coverage and energy efficiency (Ding et al., 2024; A.-T. Le et al., 2024; S. Q. Nguyen, Le, Phan, et al., 2024; X. N. Pham et al., 2024). In parallel, relay stations serve as active intermediaries that receive, process, and forward signals between IoT devices and access points, effectively extending communication range and reliability, especially in challenging environments with obstacles or deep fading. The integration of IRS and relaying techniques into IoT networks enables efficient connectivity for massive low-power devices, supporting diverse applications such as smart cities, industrial automation, environmental sensing, and intelligent transportation systems (Quang et al., 2024; Zhang et al., 2024).

In IoT-oriented wireless networks, IRSs offer several key advantages that directly address the limitations of low-power and wide-coverage communication. By intelligently adjusting the phase shifts of a large number of passive REs, IRSs can reconfigure the wireless propagation environment to enhance signal strength, suppress interference, and overcome blockages (V. D. Le et al., 2025). These capabilities enable reliable connectivity even in challenging propagation conditions. Moreover, since IRSs operate without active radio-frequency chains, they introduce negligible power consumption, making them particularly suitable for energy-constrained IoT devices. As a result, IRS-assisted communication can significantly improve link reliability, extend coverage, and reduce the required transmit power in large-scale IoT deployments (S. Q. Nguyen, Le, Phan, et al., 2024; X. N. Pham et al., 2024; Vu et al., 2025).

In addition, low-power wide-area networks (LPWANs) are recognized as a fundamental enabler of large-scale IoT deployments that require long-range communication, low power consumption, and cost-effective connectivity (Hu et al., 2024, 2025; N. Nguyen et al., 2025). Unlike traditional wireless systems such as Wi-Fi or cellular networks, LPWANs are specifically designed to support massive numbers of low-data-rate devices that operate over extended periods on small batteries. By offering wide coverage, often up to several kilometers, LPWAN technologies such as Long-Range (LoRa), Sigfox (a proprietary LPWAN protocol), and narrow-band IoT (NB-IoT) enable reliable communication for various IoT applications, including smart metering, precision agriculture, environmental monitoring, smart city infrastructures, and industrial automation. These networks facilitate efficient data collection from distributed sensors and devices, making them ideal for scenarios where energy efficiency, scalability, and low maintenance costs are essential for sustainable IoT system deployment (Alqurashi et al., 2023; Sahoo & Rai, 2025).

In recent years, considerable research efforts have focussed on analyzing wireless communication systems that integrate IRS with relay nodes to enhance network performance (Ding et al., 2024; Hedhly et al., 2024; Zhang et al., 2024). In such hybrid architectures, the IRS is generally positioned to manipulate the propagation environment and improve the quality of the source-relay transmission. However, the relay-destination link is usually established without the aid of an IRS, resulting in an asymmetric system configuration.

To evaluate the effectiveness of these designs, performance metrics in terms of outage and error probabilities are commonly derived through both analytical modelling and Monte Carlo simulations (Ding et al., 2024; Zhang et al., 2024). The obtained results consistently demonstrate that increasing the IRS's reflecting-element array size leads to noticeable improvements in signal quality and overall system reliability. Nevertheless, these gains tend to saturate when the IRS becomes sufficiently large. This performance saturation is mainly attributed to the fact that the relay-destination channel does not benefit from IRS assistance, thereby becoming the dominant limiting factor in the end-to-end transmission. Consequently, further increasing the number of REs beyond a certain point provides diminishing returns in system throughput and reliability (Hedhly et al., 2024; B. C. Nguyen et al., 2023).

As discussed earlier, although the integration of relays and IRSs has been explored to harness the benefits of both technologies, most existing works have focussed on configurations employing only a single IRS. Such setups often experience performance saturation as the number of REs increases. Specifically, such architectures inherently suffer from performance saturation because only one communication link benefits from IRS-induced passive beamforming. Recent works have attempted to mitigate this limitation by optimizing IRS placement or combining IRSs with relay nodes (Albanese et al., 2024; Chhea et al., 2025; S. Le et al., 2025); however, these approaches remain limited in fully exploiting spatial diversity and achieving robust coverage under LPWAN constraints. In contrast, our work adopts a dual-IRS configuration that simultaneously enhances both the source–relay and relay–gateway links, thereby overcoming the saturation problem commonly observed in single-IRS deployments. Moreover, we extend the analysis to LPWAN scenarios, which have been largely overlooked in the IRS literature, and we investigate key system parameters such as IRS placement, number of reflecting elements, bandwidth, and carrier frequency. These contributions collectively highlight the novelty and broaden the applicability of the proposed dual-IRS-assisted LPWAN framework.

To overcome this limitation, deploying two IRSs, one assisting the source-relay link and the other enhancing the relay-destination link, can further improve communication quality and mitigate the saturation effect. Moreover, the combination of IRSs and relays in LPWANs remains largely unexplored, despite their potential to significantly extend coverage and reduce energy consumption in large-scale IoT deployments. While several prior studies have analyzed single IRS-assisted systems (Chhea et al., 2025; Huang et al., 2025; S. Le et al., 2025; T. T. H. Le et al., 2025), they provide limited capability in exploiting spatial diversity and enhancing coverage adaptability. In contrast, our work investigates a more general dual-IRS-assisted architecture that achieves improved performance and broader applicability. Furthermore, the proposed analysis incorporates key system parameters, including number of REs, IRS placement, data transmission rate, bandwidth, and carrier frequency, that have not been comprehensively addressed in previous single IRS studies. Based on this model, we derive analytical expressions for energy efficiency (EE) and system throughput (ST). The main contributions of this paper are summarized as follows.

- A new model employing one relay station and two IRSs is proposed to enhance the ST and EE of the considered LPWAN. Closed-form analytical expressions for the ST and EE are derived under Nakagami-*m* fading conditions, and the proposed framework is

applicable to 5G and B5G systems. The accuracy of the analytical results is verified through extensive Monte-Carlo simulations conducted in MATLAB.

- Numerical and simulation results demonstrate substantial enhancements in both ST and EE compared to the traditional network without IRSs. The proposed configuration consistently achieves superior performance, highlighting the benefits of incorporating two IRSs and a relay. Moreover, the effects of key system parameters, including number of REs, IRS placement, data transmission rate, bandwidth, and carrier frequency, are thoroughly analyzed. Building on these findings, practical design recommendations are introduced to achieve higher system throughput.

The remainder of this work is structured as follows. Section 2 describes the system and signal models. Section 3 provides the analytical derivations of ST and EE. Section 4 contains the numerical and simulation results. Section 5 concludes the paper.

2. System model

Figure 1 depicts the considered LPWAN architecture that integrates IRSs and a relay to support IoT applications. In this system, an IoT sensor (S) transmits signal to an IoT gateway (G) via a wireless link, and the gateway subsequently forwards the received information to a central server (C). Owing to the large coverage area of the network, a relay (R) is employed to ensure reliable data transmission between S and G. To further enhance communication performance, two surfaces, denoted as N_1 and N_2, are strategically deployed within the LPWAN. Particularly, N_1 assists S–R channel, while N_2 aids R–G channel. The IRSs N_1 and N_2 consist of $\mathcal{L}_1$ and $\mathcal{L}_2$ REs, respectively.

Notably, IRS technology has been extensively studied in recent literature, with various works examining its design, configuration, and deployment strategies in modern wireless networks. Typical IRS architectures consist of large arrays of passive or semi-passive reflecting elements whose phase shifts can be intelligently controlled to reshape the wireless environment (Yu et al., 2024; Zhou et al., 2024). Furthermore, practical deployment considerations such as element grouping, phase quantization, placement optimization, and channel estimation procedures have been addressed to ensure efficient IRS operation in real-world systems (Albanese et al., 2024; Singh, 2025; Yoneda et al., 2025). These studies provide foundational insights into IRS behaviour and motivate the system configuration shown in Figure 1.

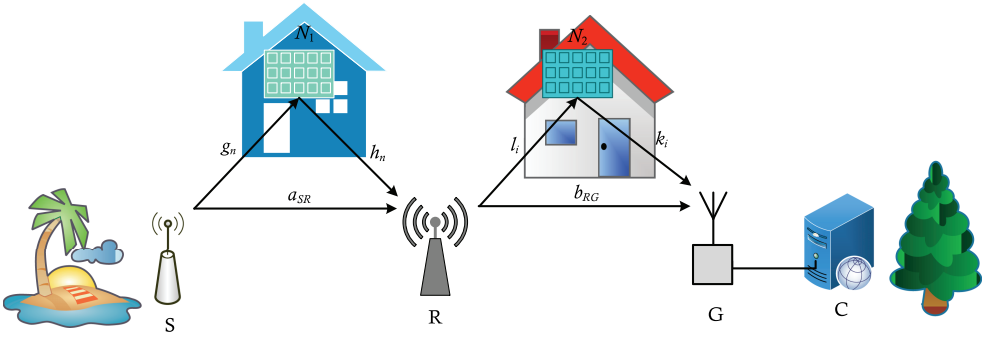

Figure 1. Block diagram of the considered LPWAN employing IRSs and a relay for IoT applications.

It is important to note that in practice, channel state information (CSI) can be obtained using pilot-based training and estimation procedures as follows. First, standard pilot sequences are transmitted to estimate the direct channels (e.g. a_{SR} and b_{RG}) using conventional pilot-assisted estimators at the receiving nodes (Lakshmi & Lakshmi, 2025; Ramesh et al., 2025). For the IRS-assisted links, the cascaded channels (e.g. $S \rightarrow N_1 \rightarrow R$ and $R \rightarrow N_2 \rightarrow G$) can be estimated by sequentially configuring the IRS phase patterns during dedicated training slots and measuring the resulting end-to-end responses at the receiver (Han et al., 2025; Ramesh et al., 2025). To reduce the large training overhead associated with configuring each reflecting element individually, practical schemes can be employed such as element grouping (controlling groups of elements with the same phase), sparse/compressed-sensing-based estimation (exploiting channel sparsity at high frequencies), and two-stage estimation procedures that first estimate aggregated (effective) channels and then refine individual components as needed. When time-division duplexing is available, channel reciprocity can further reduce training overhead by enabling uplink-based estimation of downlink channels. Alternatively, hybrid IRS architectures that incorporate a small number of sensing or active elements (semi-passive IRS) can facilitate direct channel measurements and ease estimation complexity.

The received signal at the relay can be expressed as

$$y_R = \left(a_{SR} + \sum_{n=1}^{\mathcal{L}_1} \exp(j\varphi_n) g_n h_n \right) x_S + z_R, \tag{1}$$

where x_S is the transmitted symbol from the source S with $\mathbb{E}\{|x_S|^2\} = P_S$, and P_S represents the average transmit power of S. The term z_R denotes the additive white Gaussian noise (AWGN) at R, modelled as $z_R \sim \mathcal{CN}(0, \sigma_R^2)$. The direct channel coefficient between S and R is denoted by a_{SR}, which can be written as $a_{SR} = e^{-j\phi_{SR}}|a_{SR}|$, where $|a_{SR}|$ and ϕ_{SR} represent its amplitude and phase, respectively. For the IRS-assisted link, g_n and h_n denote the complex channel coefficients from S to the nth RE of N_1 and from the nth RE of N_1 to R, respectively, while φ_n represents the phase shift applied by the nth RE. Similar to a_{SR}, these coefficients can be expressed as $g_n = e^{-j\theta_n}|g_n|$ and $h_n = e^{-j\psi_n}|h_n|$, where $|g_n|$ and $|h_n|$ denote the corresponding magnitudes, and θ_n and ψ_n denote their associated phases.

By expressing the channel coefficients in their magnitude-and-phase forms, the received signal at the relay can be rewritten as

$$\begin{aligned} y_R &= \left(|a_{SR}| e^{-j\phi_{SR}} + \sum_{n=1}^{\mathcal{L}_1} |g_n||h_n| e^{j\varphi_n - j\theta_n - j\psi_n} \right) x_S + z_R \\ &= e^{-j\phi_{SR}} \left(|a_{SR}| + \sum_{n=1}^{\mathcal{L}_1} |g_n||h_n| e^{j\lambda_n} \right) x_S + z_R, \end{aligned} \tag{2}$$

where $\lambda_n = \varphi_n + \phi_{SR} - \theta_n - \psi_n$.

According to previous studies, when perfect channel state information (CSI) is available and the IRS is equipped with intelligent control processors, each reflecting element can dynamically adjust its phase to maximize the received signal power.[1] Under this ideal condition, the optimal IRS phase shifts are chosen such that $\lambda_n = 0$, leading to the following expression for the optimal phase of the nth RE of N_1: $\varphi_n = -\phi_{SR} + \theta_n + \psi_n$.

Then, the received signal at the relay can be further simplified as

$$y_R = e^{-j\phi_{SR}}\left(|a_{SR}| + \sum_{n=1}^{\mathcal{L}_1} |g_n||h_n|\right)x_S + z_R. \tag{3}$$

Based on (3), the instantaneous signal-to-noise ratio (SNR) at the relay node R can be formulated as

$$\beta_R = \frac{\left(|a_{SR}| + \sum_{n=1}^{\mathcal{L}_1} |g_n||h_n|\right)^2 P_S |\exp(-j\phi_{SR})|^2}{\sigma_R^2}. \tag{4}$$

Since the exponential term $\exp(-j\phi_{SR})$ represents a pure phase rotation, its magnitude is unity, i.e. $|\exp(-j\phi_{SR})|^2 = 1$. Therefore, the SNR expression in (4) can be simplified to

$$\beta_R = \frac{\left(|a_{SR}| + \sum_{n=1}^{\mathcal{L}_1} |g_n||h_n|\right)^2 P_S}{\sigma_R^2}. \tag{5}$$

After successfully decoding the received signal, node R re-encodes and forwards it toward the destination node G. Consequently, the signal received at G is formulated by

$$y_G = \left(b_{RG} + \sum_{i=1}^{\mathcal{L}_2} l_i k_i e^{j\vartheta_i}\right)x_R + z_G, \tag{6}$$

where x_R denotes the information transmitted by R satisfying $\mathbb{E}\{|x_R|^2\} = P_R$; z_G denotes the AWGN at G, expressed as $z_G \sim \mathcal{CN}(0, \sigma_G^2)$; b_{RG} denotes the direct channel between R and G; l_i and k_i respectively represent the channel coefficients of the $R - i^{th}$ RE and i^{th} RE$-G$ links associated with the second IRS (N_2); and ϑ_i indicates the phase shift applied by the i^{th} reflecting element of N_2.

Analogous to the received signal at the relay node R, the signal received at the destination node G can be expressed as

$$y_G = \exp(-j\phi_{RG})\left(|b_{RG}| + \sum_{i=1}^{\mathcal{L}_2} |l_i||k_i|\right)x_R + z_G, \tag{7}$$

where ϕ_{RG} denotes the phase of the R–G channel coefficient b_{RG}.

From (7), the instantaneous SNR at G is given by

$$\begin{aligned}\beta_G &= \frac{\left(|b_{RG}| + \sum_{i=1}^{\mathcal{L}_2} |l_i||k_i|\right)^2 P_R |\exp(-j\phi_{RG})|^2}{\sigma_G^2} \\ &= \frac{\left(|b_{RG}| + \sum_{i=1}^{\mathcal{L}_2} |l_i||k_i|\right)^2 P_R}{\sigma_G^2},\end{aligned} \tag{8}$$

where the equality follows from the fact that $|\exp(-j\phi_{RG})|^2 = 1$.

Since the system employs a decode-and-forward (DF) relaying scheme, the overall end-to-end SNR of the proposed framework can be represented by

$$\beta_{\text{e2e}} = \min\{\beta_R,\ \beta_G\}. \tag{9}$$

It is important to note that all wireless links in the considered LPWAN are assumed to experience independent Nakagami-*m* fading. More specifically, the Nakagami-*m* fading model is adopted in this work due to its versatility in accurately representing a broad spectrum of wireless channel conditions encountered in practical IoT and LPWAN deployments. By adjusting the fading parameter *m*, the model can reflect environments ranging from severe multipath scattering to moderate or near line-of-sight conditions. This tunable characteristic makes Nakagami-*m* more general than Rayleigh or Rician fading and enables a unified analytical framework suitable for various operating scenarios, including dense urban areas, suburban regions, and indoor industrial IoT applications. Hence, Nakagami-*m* fading provides a realistic and mathematically tractable foundation for the system performance analysis carried out in this paper. Accordingly, the probability density function (PDF) and cumulative distribution function (CDF) of the channel amplitude, for instance $|a_{SR}|$, are respectively formulated as

$$f_{|a_{SR}|}(y) = \frac{2m_{SR}^{m_{SR}}}{\Gamma(m_{SR})\Omega_{SR}^{m_{SR}}} y^{2m_{SR}-1} \exp\left(-\frac{m_{SR}y^2}{\Omega_{SR}}\right), \tag{10}$$

and

$$\begin{aligned} F_{|a_{SR}|}(y) &= \frac{1}{\Gamma(m_{SR})}\gamma\left(m_{SR}, \frac{m_{SR}y^2}{\Omega_{SR}}\right) \\ &= 1 - \frac{1}{\Gamma(m_{SR})}\Gamma\left(m_{SR}, \frac{m_{SR}y^2}{\Omega_{SR}}\right), \end{aligned} \tag{11}$$

where m_{SR} is the fading parameter (shape factor) and Ω_{SR} is the average power gain (Tran et al., 2023).

In the following, m_g, m_h, m_{RG}, m_l, and m_k denote the fading parameters corresponding to the $S - N_1$, $N_1 - R$, R–G, $R - N_2$, and $N_2 - G$ channels, respectively. Their associated average power gains are represented as Ω_g, Ω_h, Ω_{RG}, Ω_l, and Ω_k. To accurately characterize large-scale fading, the standard 5G path-loss model is adopted as in Do et al. (2021), Yildirim et al. (2021), and B. C. Nguyen et al. (2023), given by

$$\Omega = -22.7 - 26\log(f_c) - 36.7\log(d) + \mathcal{G}_t + \mathcal{G}_r, \tag{12}$$

where f_c represents the carrier frequency (in GHz); d is the link distance between the transceiver pair (in meter); $\mathcal{G}_t$ is the antenna gain at the transmitter and $\mathcal{G}_r$ is the antenna gain at the receiver (in dB).

The corresponding noise power is expressed as

$$\sigma^2 = 10\log(B_W) + N_0 + N_F, \tag{13}$$

where B_W, N_0, and N_F represent the system bandwidth, thermal noise power density, and receiver noise figure, respectively (Tran et al., 2023).

3. System performance analysis

In evaluating the performance of LPWAN-based IoT systems, two metrics are particularly important: ST and EE. System throughput reflects the effective data transmission capability of the network and indicates how reliably IoT devices can deliver information under varying channel conditions. Meanwhile, energy efficiency measures the ratio

between successfully transmitted data and total power consumption, directly reflecting the sustainability of long-term IoT operations. Since IoT devices are typically battery-powered and required to operate for extended periods, achieving high ST while maintaining high EE is essential for practical deployment. These metrics therefore serve as key performance indicators in assessing the advantages of IRS-assisted LPWAN architectures.

3.1. System throughput analysis

System throughput quantifies the effective data transmission capability of a network, expressed in bit/s/Hz. It is a critical metric for assessing network performance and efficiency under practical operating conditions. The ST of the proposed LPWAN can be defined as

$$\mathcal{S}_{\mathcal{T}} = \mathcal{R}(1 - \mathcal{O}_{\mathcal{P}}), \tag{14}$$

where $\mathcal{R}$ is the target transmission rate and $\mathcal{O}_{\mathcal{P}}$ denotes the outage probability of the LPWAN.

The outage probability represents the likelihood that the instantaneous achievable rate falls below the target rate and can be written as

$$\mathcal{O}_{\mathcal{P}} = \Pr\left\{\frac{1}{2}\log_2(1 + \beta_{\text{e2e}}) < \mathcal{R}\right\}, \tag{15}$$

where β_{e2e} is the end-to-end SNR defined in (9). The factor 1/2 accounts for the two time slots required by the DF relaying protocol to complete one end-to-end transmission between S and G.

By rearranging (15), the outage probability can be equivalently expressed as

$$\mathcal{O}_{\mathcal{P}} = \Pr\{\beta_{\text{e2e}} < 2^{2\mathcal{R}} - 1\} = \Pr\{\beta_{\text{e2e}} < \beta_{\text{th}}\}, \tag{16}$$

where $\beta_{\text{th}} = 2^{2\mathcal{R}} - 1$ represents the SNR threshold required to achieve the target rate.

Substituting (9) into (16), we obtain

$$\mathcal{O}_{\mathcal{P}} = \Pr\{\min(\beta_R,\ \beta_G) < \beta_{\text{th}}\}. \tag{17}$$

Since β_R and β_G are statistically independent, the expression in (17) can be expanded as

$$\mathcal{O}_{\mathcal{P}} = \Pr\{\beta_R < \beta_{\text{th}}\} + \Pr\{\beta_G < \beta_{\text{th}}\} - \Pr\{\beta_R < \beta_{\text{th}}\}\Pr\{\beta_G < \beta_{\text{th}}\}. \tag{18}$$

From (18), the ST expression of the proposed LPWAN architecture can be derived as follows.

Theorem 3.1 Considering the LPWAN under Nakagami-*m* fading conditions, the ST is mathematically derived as

$$\begin{aligned}\mathcal{S}_{\mathcal{T}} = \mathcal{R} \times \exp\left(-\Psi_1\sqrt{\frac{\beta_{\text{th}}}{\bar{\beta}_R}} - \Psi_2\sqrt{\frac{\beta_{\text{th}}}{\bar{\beta}_G}}\right) \\ \times \sum_{u=0}^{\Theta_1-1}\sum_{v=0}^{\Theta_2-1}\frac{1}{u!v!}\left(\Psi_1\sqrt{\frac{\beta_{\text{th}}}{\bar{\beta}_R}}\right)^u\left(\Psi_2\sqrt{\frac{\beta_{\text{th}}}{\bar{\beta}_G}}\right)^v,\end{aligned} \tag{19}$$

where

$$\Theta_1 = \frac{[\Delta_{\mathcal{Z}_{SR}}(1)]^2}{\Delta_{\mathcal{Z}_{SR}}(2) - [\Delta_{\mathcal{Z}_{SR}}(1)]^2}, \tag{20}$$

$$\Theta_2 = \frac{[\Delta_{\mathcal{Z}_{RG}}(1)]^2}{\Delta_{\mathcal{Z}_{RG}}(2) - [\Delta_{\mathcal{Z}_{RG}}(1)]^2}, \tag{21}$$

$$\Psi_1 = \frac{\Delta_{\mathcal{Z}_{SR}}(1)}{\Delta_{\mathcal{Z}_{SR}}(2) - [\Delta_{\mathcal{Z}_{SR}}(1)]^2}, \tag{22}$$

$$\Psi_2 = \frac{\Delta_{\mathcal{Z}_{RG}}(1)}{\Delta_{\mathcal{Z}_{RG}}(2) - [\Delta_{\mathcal{Z}_{RG}}(1)]^2}. \tag{23}$$

Here, $\bar{\beta}_R = P_S/\sigma_R^2$ and $\bar{\beta}_G = P_R/\sigma_G^2$ denote the average SNRs at nodes R and G, respectively. Δ is used to denote the moment functions. The remaining parameters are specified below.

Proof. By substituting the instantaneous SNR expressions of β_R and β_G given in (5) and (8), respectively, the cumulative probabilities $\Pr\{\beta_R < \beta_{\text{th}}\}$ and $\Pr\{\beta_G < \beta_{\text{th}}\}$ can be formulated as

$$\Pr\{\beta_R < \beta_{\text{th}}\} = \Pr\left\{\frac{\left(|a_{SR}| + \sum_{n=1}^{\mathcal{L}_1} |g_n||h_n|\right)^2 P_S}{\sigma_R^2} < \beta_{\text{th}}\right\}, \tag{24}$$

$$\Pr\{\beta_G < \beta_{\text{th}}\} = \Pr\left\{\frac{\left(|b_{RG}| + \sum_{i=1}^{\mathcal{L}_2} |l_i||k_i|\right)^2 P_R}{\sigma_G^2} < \beta_{\text{th}}\right\}. \tag{25}$$

Let $\mathcal{X}_n = |g_n\|h_n|$, $\mathcal{Y}_{SR} = \sum_{n=1}^{\mathcal{L}_1} \mathcal{X}_n$, $\mathcal{Z}_{SR} = |a_{SR}| + \sum_{n=1}^{\mathcal{L}_1} |g_n\|h_n|$, $\mathcal{X}_i = |l_i\|k_i|$, $\mathcal{Y}_{RG} = \sum_{i=1}^{\mathcal{L}_2} \mathcal{X}_i$, and $\mathcal{Z}_{RG} = |b_{RG}| + \sum_{i=1}^{\mathcal{L}_2} |l_i\|k_i|$. Then, (24) and (25) can be rewritten as

$$\begin{aligned}\Pr\{\beta_R < \beta_{\text{th}}\} &= \Pr\left\{\mathcal{Z}_{SR}^2 \bar{\beta}_R < \beta_{\text{th}}\right\} = \Pr\left\{\mathcal{Z}_{SR}^2 < \frac{\beta_{\text{th}}}{\bar{\beta}_R}\right\} \\ &= F_{\mathcal{Z}_{SR}^2}\left(\frac{\beta_{\text{th}}}{\bar{\beta}_R}\right) = F_{\mathcal{Z}_{SR}}\left(\sqrt{\frac{\beta_{\text{th}}}{\bar{\beta}_R}}\right),\end{aligned} \tag{26}$$

$$\begin{aligned}\Pr\{\beta_G < \beta_{\text{th}}\} &= \Pr\left\{\mathcal{Z}_{RG}^2 \bar{\beta}_G < \beta_{\text{th}}\right\} = \Pr\left\{\mathcal{Z}_{RG}^2 < \frac{\beta_{\text{th}}}{\bar{\beta}_G}\right\} \\ &= F_{\mathcal{Z}_{RG}^2}\left(\frac{\beta_{\text{th}}}{\bar{\beta}_G}\right) = F_{\mathcal{Z}_{RG}}\left(\sqrt{\frac{\beta_{\text{th}}}{\bar{\beta}_G}}\right).\end{aligned} \tag{27}$$

Applying (Do et al., 2021), we obtain

$$\begin{aligned}\Pr\{\beta_R < \beta_{\text{th}}\} &= \frac{1}{\Gamma\left(\dfrac{[\Delta_{\mathcal{Z}_{SR}}(1)]^2}{\Delta_{\mathcal{Z}_{SR}}(2) - [\Delta_{\mathcal{Z}_{SR}}(1)]^2}\right)} \\ &\quad \times \gamma\left(\frac{[\Delta_{\mathcal{Z}_{SR}}(1)]^2}{\Delta_{\mathcal{Z}_{SR}}(2) - [\Delta_{\mathcal{Z}_{SR}}(1)]^2}, \frac{\Delta_{\mathcal{Z}_{SR}}(1)}{\Delta_{\mathcal{Z}_{SR}}(2) - [\Delta_{\mathcal{Z}_{SR}}(1)]^2}\sqrt{\frac{\beta_{\text{th}}}{\bar{\beta}_R}}\right) \\ &= \frac{1}{\Gamma(\Theta_1)}\gamma\left(\Theta_1, \Psi_1\sqrt{\frac{\beta_{\text{th}}}{\bar{\beta}_R}}\right),\end{aligned} \tag{28}$$

$$\begin{aligned}\Pr\{\beta_G < \beta_{\text{th}}\} &= \frac{1}{\Gamma\left(\dfrac{[\Delta_{\mathcal{Z}_{RG}}(1)]^2}{\Delta_{\mathcal{Z}_{RG}}(2) - [\Delta_{\mathcal{Z}_{RG}}(1)]^2}\right)} \\ &\quad \times \gamma\left(\frac{[\Delta_{\mathcal{Z}_{RG}}(1)]^2}{\Delta_{\mathcal{Z}_{RG}}(2) - [\Delta_{\mathcal{Z}_{RG}}(1)]^2}, \frac{\Delta_{\mathcal{Z}_{RG}}(1)}{\Delta_{\mathcal{Z}_{RG}}(2) - [\Delta_{\mathcal{Z}_{RG}}(1)]^2}\sqrt{\frac{\beta_{\text{th}}}{\bar{\beta}_G}}\right) \\ &= \frac{1}{\Gamma(\Theta_2)}\gamma\left(\Theta_2, \Psi_2\sqrt{\frac{\beta_{\text{th}}}{\bar{\beta}_G}}\right),\end{aligned} \tag{29}$$

where

$$\Delta_{\mathcal{Z}_{SR}}(1) = \Delta_{|a_{SR}|}(1) + \Delta_{\mathcal{Y}_{SR}}(1), \tag{30}$$

$$\Delta_{\mathcal{Z}_{SR}}(2) = \Delta_{|a_{SR}|}(2) + \Delta_{\mathcal{Y}_{SR}}(2) + 2\Delta_{|a_{SR}|}(1)\Delta_{\mathcal{Y}_{SR}}(1), \tag{31}$$

$$\Delta_{\mathcal{Z}_{RG}}(1) = \Delta_{|b_{RG}|}(1) + \Delta_{\mathcal{Y}_{RG}}(1), \tag{32}$$

$$\Delta_{\mathcal{Z}_{RG}}(2) = \Delta_{|b_{RG}|}(2) + \Delta_{\mathcal{Y}_{RG}}(2) + 2\Delta_{|b_{RG}|}(1)\Delta_{\mathcal{Y}_{RG}}(1), \tag{33}$$

$$\Delta_{|a_{SR}|}(1) = \sqrt{\frac{\Omega_{SR}}{m_{SR}}} \times \frac{\Gamma(m_{SR} + 1/2)}{\Gamma(m_{SR})}, \tag{34}$$

$$\Delta_{|a_{SR}|}(2) = \frac{\Omega_{SR}}{m_{SR}} \times \frac{\Gamma(m_{SR} + 1)}{\Gamma(m_{SR})} = \Omega_{SR}, \tag{35}$$

$$\Delta_{|b_{RG}|}(1) = \sqrt{\frac{\Omega_{RG}}{m_{RG}}} \times \frac{\Gamma(m_{RG} + 1/2)}{\Gamma(m_{RG})}, \tag{36}$$

$$\Delta_{|b_{RG}|}(2) = \Omega_{RG}. \tag{37}$$

$$\Delta_{\mathcal{Y}_{SR}}(1) = \sum_{n=1}^{\mathcal{L}_1} \Delta_{\mathcal{X}_n}(1), \tag{38}$$

$$\Delta_{\mathcal{Y}_{SR}}(2) = \sum_{n=1}^{\mathcal{L}_1} \Delta_{\mathcal{X}_n}(2) + 2\sum_{n=1}^{\mathcal{L}_1}\sum_{n'=n+1}^{\mathcal{L}_1} [\Delta_{\mathcal{X}_n}(1)]^2, \tag{39}$$

$$\Delta_{\mathcal{Y}_{RG}}(1) = \sum_{i=1}^{\mathcal{L}_2} \Delta_{\mathcal{X}_i}(1), \tag{40}$$

$$\Delta_{\mathcal{Y}_{RG}}(2) = \sum_{i=1}^{\mathcal{L}_2} \Delta_{\mathcal{X}_i}(2) + 2\sum_{i=1}^{\mathcal{L}_2}\sum_{i'=i+1}^{\mathcal{L}_2} [\Delta_{\mathcal{X}_i}(1)]^2. \tag{41}$$

It is because $\gamma(n, a) + \Gamma(n, a) += \Gamma(n)$, we can derive

$$\Pr\{\beta_R < \beta_{\text{th}}\} = 1 - \frac{1}{\Gamma(\Theta_1)}\Gamma\left(\Theta_1, \Psi_1\sqrt{\frac{\beta_{\text{th}}}{\bar{\beta}_R}}\right), \tag{42}$$

$$\Pr\{\beta_G < \beta_{\text{th}}\} = 1 - \frac{1}{\Gamma(\Theta_2)}\Gamma\left(\Theta_2, \Psi_2\sqrt{\frac{\beta_{\text{th}}}{\bar{\beta}_G}}\right). \tag{43}$$

Now, using $\Gamma(a, x) = \Gamma(a)e^{-x}\sum_{t=0}^{a-1}\frac{1}{t!}x^t$, (42) and (43) become

$$\Pr\{\beta_R < \beta_{\text{th}}\} = 1 - \exp\left(-\Psi_1\sqrt{\frac{\beta_{\text{th}}}{\bar{\beta}_R}}\right)\sum_{u=0}^{\Theta_1-1}\frac{1}{u!}\left(\Psi_1\sqrt{\frac{\beta_{\text{th}}}{\bar{\beta}_R}}\right)^u, \tag{44}$$

$$\Pr\{\beta_G < \beta_{\text{th}}\} = 1 - \exp\left(-\Psi_2\sqrt{\frac{\beta_{\text{th}}}{\bar{\beta}_G}}\right)\sum_{v=0}^{\Theta_2-1}\frac{1}{v!}\left(\Psi_2\sqrt{\frac{\beta_{\text{th}}}{\bar{\beta}_G}}\right)^v. \tag{45}$$

Consequently, we obtain

$$\begin{aligned}\mathcal{O}_{\mathcal{P}} \approx 1 - \exp&\left(-\Psi_1\sqrt{\frac{\beta_{\text{th}}}{\bar{\beta}_R}} - \Psi_2\sqrt{\frac{\beta_{\text{th}}}{\bar{\beta}_G}}\right)\\ &\times \sum_{u=0}^{\Theta_1-1}\sum_{v=0}^{\Theta_2-1}\frac{1}{u!v!}\left(\Psi_1\sqrt{\frac{\beta_{\text{th}}}{\bar{\beta}_R}}\right)^u\left(\Psi_2\sqrt{\frac{\beta_{\text{th}}}{\bar{\beta}_G}}\right)^v.\end{aligned} \tag{46}$$

By inserting (46) into (14), we derive the result presented in (19), thereby completing the proof.

3.2. Energy efficiency analysis

The EE of the LPWAN can be expressed as T. H. T. Pham et al. (2025)

$$\mathcal{E}_{\text{E}} = \frac{B_W\mathcal{S}_{\mathcal{T}}}{P_{\text{all}}}, \tag{47}$$

where B_W denotes the system bandwidth, $\mathcal{S}_{\mathcal{T}}$ represents the system throughput, and P_{all} corresponds to the total power consumption of the LPWAN.

Based on (47), the analytical expression for the EE of the proposed LPWAN is derived as follows.

Theorem 3.2 Considering the LPWAN under Nakagami-*m* fading conditions, the EE is expressed by

$$\mathcal{E}_{\mathrm{E}} = \frac{\mathcal{R}B_W}{P_{\mathrm{all}}} \exp\left(-\Psi_1\sqrt{\frac{\beta_{\mathrm{th}}}{\bar{\beta}_R}} - \Psi_2\sqrt{\frac{\beta_{\mathrm{th}}}{\bar{\beta}_G}}\right) \times \sum_{u=0}^{\Theta_1-1}\sum_{v=0}^{\Theta_2-1} \frac{1}{u!v!}\left(\Psi_1\sqrt{\frac{\beta_{\mathrm{th}}}{\bar{\beta}_R}}\right)^u \left(\Psi_2\sqrt{\frac{\beta_{\mathrm{th}}}{\bar{\beta}_G}}\right)^v, \tag{48}$$

where

$$P_{\mathrm{all}} = P_S + P_R + \tilde{P}_S + 2\tilde{P}_R + \tilde{P}_G + \sum_{n=1}^{\mathcal{L}_1}\tilde{P}_n + \sum_{i=1}^{\mathcal{L}_2}\tilde{P}_i, \tag{49}$$

where $\tilde{P}_S$, $\tilde{P}_R$, $\tilde{P}_G$, $\tilde{P}_n$, and $\tilde{P}_i$ denote the circuit dissipation power at S, R, G n^{th} RE, and i^{th} RE, respectively.

Proof. Following the approach in Do et al. (2021), the total consumed power P_{all} of the LPWAN is given in (49). By substituting (19) into (47), the EE expression of the proposed framework is derived as shown in (48). Hence, the proof is complete.

4. Results and discussions

This section investigates the EE and ST of the proposed system under various operating conditions. Both theoretical analyses and Monte-Carlo simulations are conducted to verify the accuracy of the derived formulas. In the following figures, the term 'Wi-IRS' refers to the performance of the proposed LPWAN incorporating IRSs and a relay, whereas 'Wo-IRS' denotes the conventional LPWAN employing only a relay, without IRS assistance. Since the proposed architecture differs fundamentally from existing system models, the performance comparison is limited to the cases with and without IRS deployment to clearly emphasize the benefits of integrating IRS technology. The main simulation parameters are configured as follows: $d_{\mathrm{SR}} = d_{\mathrm{RG}} = 100$ [m], $N_F = 10$ [dB] and $N_0 = -174$ [dBm/Hz] (for the computation of σ^2 in (13)); $\mathcal{G}_t = \mathcal{G}_r = 5$ [dB] (for calculating the average channel gain in (12)); $m_l = m_k = m_g = m_h = m_{SR} = m_{RG} = 2$; and $P_{\mathrm{tx}} = P_S = P_R$. Other system parameters are adjusted as needed to illustrate the performance characteristics of the LPWAN under different scenarios. For improved readability, all simulation parameters are summarized in Table 1.

Figure 2 illustrates the ST of the proposed framework versus transmit power P_{tx} with target rate $\mathcal{R} = 2$ bit/s/Hz, $\mathcal{L}_1 = \mathcal{L}_2 = 40$ REs, bandwidth $B_W = 10$ MHz, carrier frequency $f_c = 3$ GHz, and different positions of N_1 and N_2. More specifically, we set $d_{SN_1} = d_{RN_2} = 10$, 20, 30, 40, and 50 m. In other words, N_1 moves from a position close to S to a position between S and R. Meanwhile, N_2 moves from a position close to R to a position between R and G. The other parameters are presented as above. In Figure 2, the theoretical ST of the proposed framework is obtained by using (19), and the ST of the other one without IRS is shown for comparison. The analytical and Monte-Carlo

results closely coincide, validating the derived expression. On the other hand, the ST of the LPWAN with IRSs is considerably higher than the ST of the LPWAN without IRS. This feature shows the gains achieved by using IRSs in the LPWAN. In addition, when N_1 is close to S and N_2 is close to R ($d_{SN_1} = d_{RN_2} = 10$ m), the ST of the proposed LPWAN is the best. Conversely, the ST of the proposed LPWAN is the worst when N_1 is between S and R, and N_2 is between R and G ($d_{SN_1} = d_{RN_2} = 50$ m). This characteristic of the IRS is different from traditional relays because traditional relays often provide the best quality when they are located between the transmitter and receiver. Note that in addition to placing the IRS near the transmitter (N_1 close to S and N_2 close to R), we can place the IRS near the receiver (N_1 close to R and N_2 close to G) to achieve similar performance.

Figure 3 presents the performance comparison of the LPWAN with and without IRSs under different carrier frequencies, namely $f_c = 2.4$, 3.4, and 5 GHz. It can be seen that higher operating frequencies lead to a noticeable degradation in throughput, which aligns well with the analytical relationship in (12). For instance, when $P_{\text{tx}} = 10$ dBm, the proposed LPWAN achieves approximately 2 bits/s/Hz at 2.4 GHz, but the throughput drops to nearly 0 bits/s/Hz at 5 GHz. This indicates that, at a fixed transmission power of 10 dBm, an increase in f_c, i.e. from 2.4 GHz to 5 GHz results in a throughput reduction from 2 bits/s/Hz to 0 bits/s/Hz. In terms of power efficiency, the proposed framework operating at 5 GHz requires roughly 15 dBm higher transmit power to attain the same throughput achieved at 2.4 GHz. A similar trend is observed for the traditional LPWAN without IRSs. Specifically, at 5 GHz, its throughput only achieves 1.1 bits/s/Hz even when $P_{\text{tx}} = 30$ dBm. Therefore, when employing high-frequency bands such as 5 GHz, the conventional LPWAN struggles to achieve the desired throughput, regardless of increased power. These findings emphasize the importance of selecting an appropriate carrier frequency to ensure high throughput with minimal transmission power in both proposed and conventional LPWAN configurations.

Figure 4 analyzes the influence of B_W on the throughput performance of both the proposed and conventional LPWANs, where B_W is varied (1 MHz → 10 MHz). We investigate three transmit power levels, namely $P_{\text{tx}} = 10$, 15, and 20 dBm, while other parameters remain consistent with those used in Figure 3. As B_W increases, the corresponding noise power also rises, as indicated by (13), resulting in a notable degradation in throughput. For instance, when $P_{\text{tx}} = 10$ dBm, the throughput of the proposed and traditional

Table 1. Simulation parameters for the proposed LPWAN framework.

Parameter	Value/Description
Carrier frequency (f_c)	2.4–5 GHz (varied)
Bandwidth (BW)	1–10 MHz (varied)
Transmit power (P_{tx})	10–30 dBm (varied)
Thermal noise density (N_0)	−174 dBm/Hz
Noise figure (N_F)	10 dB
Antenna gains ($\mathcal{G}_t$, $\mathcal{G}_r$)	5 dB each
Path-loss model	3GPP Urban Macro
Distances	$d_{SR} = d_{RG} = 100$ m
IRS positions	d_{SN_1}, d_{RN_2} varied from 10–50 m
Number of REs ($\mathcal{L}_1$, $\mathcal{L}_2$)	20, 40, 60, 80, 100 (varied)
Fading parameters (m)	$m_l = m_k = m_g = m_h = m_{SR} = m_{RG} = 2$
Noise variances ($\sigma^2_{R_\mathcal{L}}$ $\sigma^2_{\mathcal{G}}$)	Computed via (13)
Circuit powers (P_S, P_R, P_G)	Included as in (49)
Monte-Carlo runs	10^6 samples per point

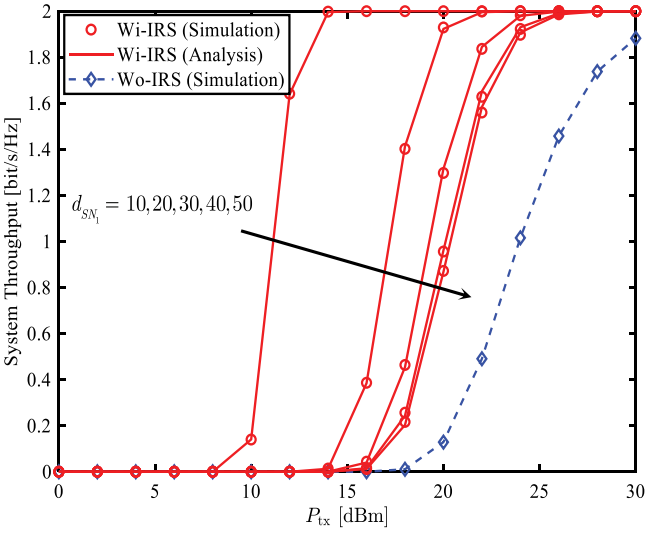

Figure 2. The ST of the proposed framework versus transmit power P_{tx} with target rate $\mathcal{R} = 2$ bit/s/Hz, $\mathcal{L}_1 = \mathcal{L}_2 = 40$ REs, bandwidth $B_W = 10$ MHz, carrier frequency $f_c = 3$ GHz, and various positions of IRSs N_1 and N_2.

LPWANs decreases from approximately 1.9 to 1.0 and 0.6 to 0.05 bits/s/Hz, respectively, as B_W increases from 1 MHz to 2 MHz. This clearly demonstrates that, under fixed conditions, a larger bandwidth leads to reduced throughput because of increased noise power. Similar tendencies are observed at $P_{\text{tx}} = 15$ and 20 dBm. Hence, to maximize throughput performance, it is essential to appropriately balance key design factors such as number of REs, transmission rate, IRS placement, bandwidth, and carrier frequency.

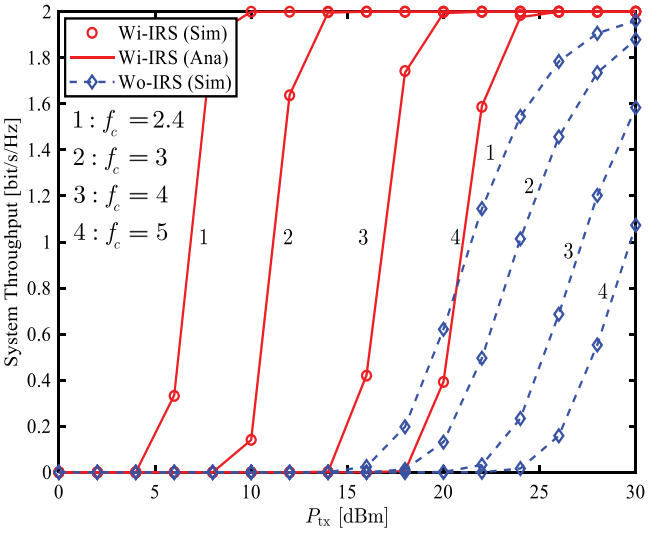

Figure 3. The ST of the LPWAN versus transmit power P_{tx} with $\mathcal{R} = 2$ bit/s/Hz, $B_W = 10$ MHz, $\mathcal{L}_1 = \mathcal{L}_2 = 40$ REs, and $d_{SN_1} = d_{RN_2} = 50$ m.

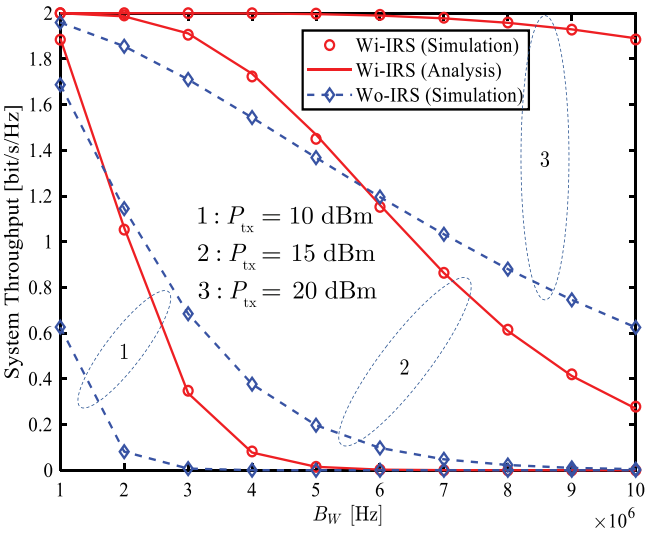

Figure 4. The ST of the LPWAN versus bandwidth B_W with $\mathcal{R} = 2$ bit/s/Hz, $P_{tx} = 10$, 15, and 20 dBm, $\mathcal{L}_1 = \mathcal{L}_2 = 40$ REs, and $d_{SN_1} = d_{RN_2} = 50$ m.

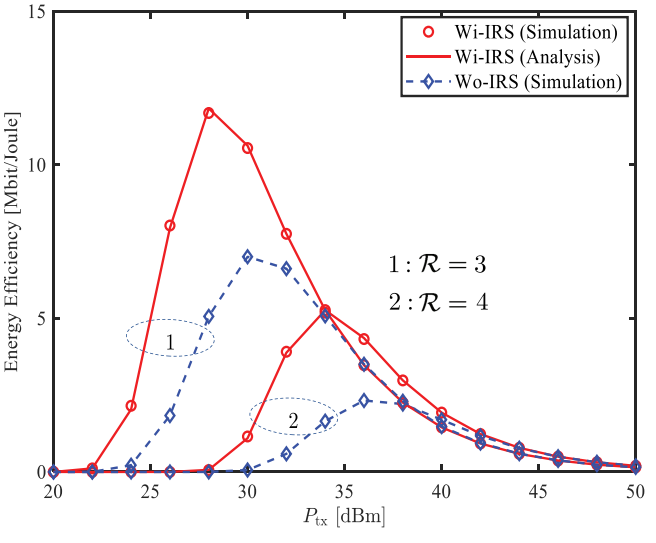

Figure 5. The EE of the LPWAN versus transmit power P_{tx} with $\mathcal{R} = 3$, 4 bit/s/Hz, $B_W = 10$ MHz, $f_c = 3$ GHz, $\mathcal{L}_1 = \mathcal{L}_2 = 40$ REs, and $d_{SN_1} = d_{RN_2} = 50$ m.

Figure 5 presents the energy efficiency of the proposed framework as a function of P_{tx}. The analytical results for the system employing IRSs are obtained from (48). As observed, the maximum energy efficiency achieved with IRSs is significantly higher than that of the configuration without IRSs. Specifically, the peak values reach approximately 11.8 and 5.1 bits/s/Hz for $\mathcal{R} = 3$ and 4 bits/s/Hz, respectively, whereas the corresponding values for the system without IRSs are only 7 and 2.3 bits/s/Hz. Furthermore, the proposed system achieves its optimal energy efficiency at a lower transmit power compared to the

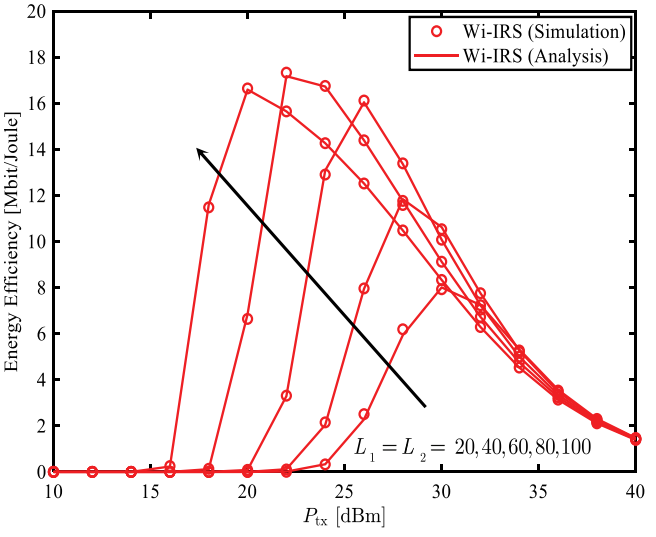

Figure 6. The EE of the LPWAN is evaluated for various values of $\mathcal{L}_1$ and $\mathcal{L}_2$, considering $\mathcal{R} = 2$ bits/s/Hz, $f_c = 3$ GHz, and $d_{SN_1} = d_{RN_2} = 50$ m.

conventional setup. These results clearly indicate that incorporating two IRSs into the LPWAN architecture can substantially enhance energy efficiency while simultaneously reducing power consumption.

Figure 6 depicts the energy efficiency performance of the LPWAN for various values of $\mathcal{L}_1$ and $\mathcal{L}_2$, where $\mathcal{L}_1 = \mathcal{L}_2 = 20$, 40, 60, 80, and 100 reflecting elements. It is evident that increasing the number of reflecting elements significantly reduces the transmit power necessary to achieve the optimal energy efficiency. This behaviour highlights that enlarging the size of the intelligent reflecting surfaces enables the network to operate with greater efficiency and decreased transmit power. In other words, employing larger IRSs enhances the signal reflection and propagation quality, thereby improving energy efficiency and reducing overall power consumption.

5. Conclusion

This work presented an IoT-oriented LPWAN architecture integrating IRSs and a relay to enhance communication performance. By employing rigorous analytical derivations, closed-form expressions for the system throughput and energy efficiency were obtained under realistic 5G and beyond channel models. Numerical evaluations confirmed that the proposed LPWAN, equipped with dual IRSs, achieves remarkable improvements in both throughput and energy efficiency compared to conventional relay-based LPWANs without IRSs. The performance gains become more pronounced as the number of reflecting elements increases. Moreover, extensive analyses were conducted to examine the influence of key system parameters, including the number and placement of reflecting elements, transmission rate, carrier frequency, and bandwidth. The insights derived from these analyses provide practical guidelines for optimizing LPWAN design and deployment to maximize throughput and energy efficiency in future IoT networks.[2]

Notes

1. The analysis in this paper assumes perfect CSI and ideal hardware to provide a theoretical performance benchmark. In practice, imperfections such as CSI estimation errors, synchronization mismatches, and hardware impairments (e.g. non-ideal IRS phase responses or amplifier nonlinearities) may degrade performance. Future research may extend this work by incorporating robustness analysis frameworks to quantify such effects and propose corresponding mitigation strategies (T. P. Nguyen et al., 2025).
2. In real-world deployments, several factors may impact the performance of the proposed system. For instance, user or object mobility can lead to rapid variations in channel conditions, which may challenge the system's ability to maintain optimal IRS configurations. Environmental obstructions, such as buildings or foliage, may block or degrade reflected signals, reducing the effectiveness of IRS-assisted communication. Furthermore, hardware impairments such as phase noise, quantization errors in IRS elements, and limited-resolution phase shifters, can introduce performance degradation compared to the idealized assumptions in our analysis. These practical limitations highlight the importance of developing robust channel estimation and IRS control strategies, which are promising directions for future research.

Disclosure statement

No potential conflict of interest was reported by the author(s).

ORCID

Tan N. Nguyen http://orcid.org/0000-0002-2286-6652

References

Albanese, A., Devoti, F., Sciancalepore, V., Di Renzo, M., Banchs, A., & Costa-Pérez, X. (2024). ARES: Autonomous RIS solution with energy harvesting and self-configuration towards 6G. *IEEE Transactions on Mobile Computing*, *23*(12), 12006–12019. https://doi.org/10.1109/TMC.2024.3405076

Alqurashi, H., Bouabdallah, F., & Khairullah, E. (2023). SCAP sigfox: A scalable communication protocol for low-power wide-area IoT networks. *Sensors*, *23*(7), 1–23. https://doi.org/10.3390/s23073732

Chhea, K., Muy, S., & Lee, J. (2025). Energy efficiency optimization in intelligent reflecting surface-aided UAV wireless power transfer networks using DRL. *IEEE Transactions on Vehicular Technology*, *74*(4), 6599–6609. https://doi.org/10.1109/TVT.2024.3519591

Ding, Q., Yang, J., Luo, Y., & Luo, C. (2024). Intelligent reflecting surfaces vs. full-duplex relays: A comparison in the air. *IEEE Communications Letters*, *28*(2), 397–401. https://doi.org/10.1109/LCOMM.2023.3344599

Do, T. N., Kaddoum, G., Nguyen, T. L., da Costa, D. B., & Haas, Z. J. (2021). Multi-RIS-aided wireless systems: Statistical characterization and performance analysis. *IEEE Communications Letters*, *69*(12), 8641–8658.

Han, S., Liao, Y., Chen, S., & Liang, Y. (2025). Joint channel estimation for RIS-aided mmwave MIMO wireless communication systems with mixed-resolution quantization schemes. *IEEE Internet of Things Journal*, *12*(16), 33756–33768. https://doi.org/10.1109/JIOT.2025.3576287

Hedhly, W., Amin, O., Alouini, M., & Shihada, B. (2024). Intelligent reflecting surfaces assisted hyperloop wireless communication network. *IEEE Transactions on Mobile Computing*, *23*(5), 4943–4955. https://doi.org/10.1109/TMC.2023.3299792

Hu, Y., Jin, H., & Seo, J. (2024). Asynchronous random access systems with immediate collision resolution for low power wide area networks. *IEEE Transactions on Vehicular Technology*, *73*(2), 2755–2770. https://doi.org/10.1109/TVT.2023.3320353

Hu, Y., Seo, J., & Jin, H. (2025). The effect of imperfect channel sensing for low-power wide-area networks with listen-before-talk. *IEEE Internet of Things Journal*, *12*(12), 20512–20529. https://doi.org/10.1109/JIOT.2025.3543799

Huang, Q., Hu, J., & Yang, K. (2025). Intelligent reflecting surface assisted integrated data and energy multicast system in terahertz-bands. *IEEE Transactions on Green Communications and Networking*, *9*(1), 152–163. https://doi.org/10.1109/TGCN.2024.3415030

Lakshmi, N. D. N., & Lakshmi, B. V. (2025). HEBE optimized Mob-LSTM for channel estimation in RIS-assisted mmwave MIMO system. *International Journal of Communication Systems*, *38*(3), e6071.

Le, A.-T., Vu, T.-H., Nguyen, T. N., Tien, T.-L., & Voznak, M. (2024). Partial multiplexing power-frequency multiple access for active STAR-RIS systems: Outage and ergodic perspectives. *IEEE Wireless Communications Letters, 14*(3), 786–790.

Le, S., Nguyen, T. N., Le-Tien, T., Duy, T. T., Nguyen, T., Ng, D. W. K., Tu, L., & Voznák, M. (2025). On the secrecy performance of reconfigurable intelligent surfaces-assisted satellite networks under shadow-rician channels. *IEEE Transactions on Aerospace and Electronic Systems*, *61*(3), 6794–6808. https://doi.org/10.1109/TAES.2025.3532227

Le, T. T. H., Hoang, T. M., Tran, X. N., Hiep, P. T., & Nguyen, B. C. (2025). Enhancing the performance of the aerial relay system through rate-splitting multiple access and reconfigurable intelligent surface. *IEEE Transactions on Aerospace and Electronic Systems*, *61*(3), 7497–7511. https://doi.org/10.1109/TAES.2025.3539649

Le, V. D., Nguyen, H. N., Nguyen, S. Q., Bui, T. T., Hien, D. C., & Kim, B. S. (2025). Enabling D2D transmission mode of reconfigurable intelligent surfaces aided in wireless NOMA system. *Advances in Electrical and Electronic Engineering*, *23*(1), 32–42. https://doi.org/10.15598/aeee.v23i1.240809

Mahbub, M., & Shubair, R. M. (2024). On the analyses of propagation characteristics and user association for sub-6 GHz and mmwave carriers in intelligent reflecting surfaces-assisted multi-tier 6G networks. *International Journal of Wireless Information Networks*, *31*(1), 1–11. https://doi.org/10.1007/s10776-023-00612-y

Nguyen, B. C., Phuong, N. T., Tran, X. N., & Hiep, P. T. (2023). On performance of RIS-aided ground-to-air and air-to-ground communications in multi-user NOMA systems. *Computer Network*, *228*,109754. https://doi.org/10.1016/j.comnet.2023.109754

Nguyen, N., Nguyen, H., & Minh-Vu, B. U. I. (2025). Performance analysis of RIS-equipped UAV communication network under hardware impairments. *Advances in Electrical and Electronic Engineering*, *23*(3), 204–212.

Nguyen, S. Q., Le, A. T., Phan, V. D., Thien, H. T., & Kharel, R. (2024). Outage performance analysis of STAR-RIS-NOMA networks under imperfect CSI. *Advances in Electrical and Electronic Engineering*, *22*(3), 260–270. https://doi.org/10.15598/aeee.v22i3.5546

Nguyen, S. Q., Le, A. T., Thien, H. T., & Kharel, R. (2024). Outage performance analysis of STAR-RIS-NOMA networks under imperfect CSI. *Advances in Electrical and Electronic Engineering*, *22*(3), 260–270. https://doi.org/10.15598/aeee.v22i3.5546

Nguyen, T. P., Vo, D. T., Quang-Sy, V. U., Minh, T. R. A. N., Nguyen, Q. S., & Taejoon, K. I. M. (2025). RIS-aided multi-antenna IoT systems: Performance evaluation under MRC combining. *Advances in Electrical and Electronic Engineering*, *23*(3), 227–236.

Pham, T. H. T., Nguyen, N. T. T., Nguyen, Q. S., Nguyen, T. H., MINH, B. V., Nguyen, Q. S., & Tran, M. (2025). Performance analysis in D2D partial NOMA-assisted backscatter communication. *Advances in Electrical and Electronic Engineering*, *23*(3), 250–262. https://doi.org/10.15598/aeee.v23i3.250314

Pham, X. N., Nguyen, B. C., Thi, T. D., Van Vinh, N., Minh, B. V., Kim, T., Nguyen, T. N., & Le, A. V. (2024). Enhancing data rate and energy efficiency of NOMA systems using reconfigurable intelligent surfaces for millimeter-wave communications. *Digital Signal Processing*, *151*, Article 104553. https://doi.org/10.1016/j.dsp.2024.104553

Quang, P. M., Kien, N. T., Duy, T. T., An, N. H., Tung, N. T., & Le, A. -V. (2024). Performance evaluation of reconfigurable intelligent surface aided multi-hop relaying schemes with short packet

communication. *Advances in Electrical and Electronic Engineering*, *22*(1), 97–106. https://doi.org/10.15598/aeee.v22i1.5583

Ramesh, B., Saravanan, D., Raja, A., & Lakshmi, T. R. V. (2025). RIS-aided MISO channel estimation using fuzzy embedded recurrent neural network and binary kepler optimization algorithm. *International Journal of Communication Systems*, *38*(8), e70094. https://doi.org/10.1002/dac.v38.8

Sahoo, M., & Rai, S. (2025). A method for detection of low frequency oscillatory modes in power system for wide area monitoring system. *Computers & Electrical Engineering*, *123*, Article 110172. https://doi.org/10.1016/j.compeleceng.2025.110172

Singh, R. (2025). Native AI-integrated RIS-THz systems for intelligent and sustainable 6G RANs. *IEEE Access*, *13*,196848–196867. https://doi.org/10.1109/ACCESS.2025.3634474

Tran, P. T., Nguyen, B. C., Hoang, T. M., & Nguyen, T. N. (2023). On performance of low-power wide-area networks with the combining of reconfigurable intelligent surfaces and relay. *IEEE Transactions on Mobile Computing*, *22*(10), 6086–6096. https://doi.org/10.1109/TMC.2022.3186394

Vu, D. T., Nguyen, B. C., Nguyen, D. K., Kim, T., Minh, B. V., & Le, A. V. (2025). Enhancing mmwave performance: Multi-RIS and antenna selection under hardware impairments. *Digital Signal Processing*, *166*, Article 105389. https://doi.org/10.1016/j.dsp.2025.105389

Yildirim, I., Uyrus, A., & Basar, E. (2021). Modeling and analysis of reconfigurable intelligent surfaces for indoor and outdoor applications in future wireless networks. *IEEE Trans. Commun*. *69*(2), 1290–1301. https://doi.org/10.1109/TCOMM.26

Yoneda, T., Murakami, T., Takatori, Y., & Ogawa, T. (2025). Experimental evaluation of distributed reconfigurable intelligent surfaces control for green wireless networks. *IEEE Open Journal of the Communications Society*, *6*, 9736–9747. https://doi.org/10.1109/OJCOMS.2025.3633316

Yu, Z., Ren, H., Pan, C., Zhou, G., Wang, B., Dong, M., & Wang, J. (2024). Active RIS-aided ISAC systems: Beamforming design and performance analysis. *IEEE Transactions on Communications*, *72*(3), 1578–1595. https://doi.org/10.1109/TCOMM.2023.3332856

Zhang, L., Zhai, C., Zheng, L., & Si, W. (2024). Dual intelligent reflecting surfaces aided decode-and-forward relaying with wireless power transfer. *Transactions on Emerging Telecommunications Technologies*, *35*(1), e4901.

Zhou, G., Pan, C., Ren, H., Xu, D., Zhang, Z., Wang, J., & Schober, R. (2024). A framework for transmission design for active RIS-aided communication with partial CSI. *IEEE Transactions on Wireless Communications*, *23*(1), 305–320. https://doi.org/10.1109/TWC.2023.3277514

Appendices

Appendix 1. Pseudo-code for IRS-assisted LPWAN system model

Table A1. IRS-Assisted LPWAN System Model

Input: Distances d_{SR}, d_{RG}, d_{SN_1}, d_{RN_2}; number of REs $\mathcal{L}_1$, $\mathcal{L}_2$; transmit powers P_S, P_R; fading parameters.
Compute large-scale fading using path-loss model (Equation (12)).
for each realization $k = 1$ to N Monte-Carlo runs
Generate small-scale fading coefficients:
  a_{SR}, $b_{RG} \sim$ Nakagami$-m$
  g_n, h_n for $n = 1..\mathcal{L}_1$; l_i, k_i for $i = 1..\mathcal{L}_2$.
Compute cascaded channel gains:
  $\mathcal{X}_n = |g_n \| h_n|$, $Y_{SR} = \sum \mathcal{X}_n$
  $\mathcal{X}_i = |l_i \| k_i|$, $Y_{RG} = \sum \mathcal{X}_i$
Configure IRS phases for coherent signal combining:
  $\varphi_n^{\star} = -\phi_{SR} + \theta_n + \psi_n$
  $\vartheta_i^{\star} = -\phi_{RG} + \xi_i + \eta_i$
Compute instantaneous SNRs using Equations (5) and (8):
  $\beta_R = (|a_{SR}| + Y_{SR})^2 P_S / \sigma_R^2$
  $\beta_G = (|b_{RG}| + Y_{RG})^2 P_R / \sigma_G^2$
Compute end-to-end SNR:
  $\beta_{e2e}(k) = \min(\beta_R, \beta_G)$
end for
Output: SNR samples $\beta_{e2e}(1..N)$

Appendix 2. Pseudo-code for system throughput analysis

Table A2. Analytical System Throughput Computation

1: **Input:** Target rate $\mathcal{R}$, average SNRs $\bar{\beta}_R$, $\bar{\beta}_G$, Nakagami moments from Equations (20)–(23).
2: Compute SNR threshold: $\beta_{\text{th}} = 2^{2\mathcal{R}} - 1$.
3: Compute shape parameters:
4: $\quad \Theta_1, \Theta_2$ using Equations (20)–(21)
5: Compute scaling factors:
6: $\quad \Psi_1, \Psi_2$ using Equations (22)–(23)
7: Evaluate outage probability using Equation (46):

8: $\quad \mathcal{O}_{\mathcal{P}} = 1 - e^{-(\Psi_1\sqrt{\beta_{th}/\bar{\beta}_R}+\Psi_2\sqrt{\beta_{th}/\bar{\beta}_G})}$

9: $\times \sum_{u=0}^{\Theta_1-1} \sum_{v=0}^{\Theta_2-1} 10: \frac{(\Psi_1\sqrt{\beta_{th}/\bar{\beta}_R})^u}{u!} 11: \frac{(\Psi_2\sqrt{\beta_{th}/\bar{\beta}_G})^v}{v!}$

12: Compute system throughput:
13: $\quad \mathcal{S}_{\mathcal{T}} = \mathcal{R}(1 - \mathcal{O}_{\mathcal{P}})$
14: **Output:** Analytical throughput $\mathcal{S}_{\mathcal{T}}$